The Astrophysical Journal, 859:104 (10pp), 2018 June 1 https://doi.org/10.3847/1538-4357/aac016

Simulation of the Solar Wind Dynamic Pressure Increase in 2014 and Its Effect on Energetic Neutral Atom Fluxes from the Heliosphere

E. J. Zirnstein[1], J. Heerikhuisen[2], D. J. McComas[1], N. V. Pogorelov[2], D. B. Reisenfeld[3], and J. R. Szalay[1]
[1] Department of Astrophysical Sciences, Princeton University, Princeton, NJ 08544, USA; ejz@princeton.edu
[2] Department of Space Science, University of Alabama in Huntsville, Huntsville, AL 35899, USA
[3] University of Montana, Missoula, MT 59812, USA
Received 2018 March 10; revised 2018 April 23; accepted 2018 April 23; published 2018 May 30

Abstract

In late 2014, the solar wind dynamic pressure increased by ∼50% over a relatively short time (∼6 months). In early 2017, the *Interstellar Boundary Explorer* (*IBEX*) observed an increase in heliospheric energetic neutral atom (ENA) fluxes from directions near the front of the heliosphere. These enhanced ENA emissions resulted from the increase in SW pressure propagating through the inner heliosheath (IHS), affecting the IHS plasma pressure and emission of ∼keV ENA fluxes. We expand on the analysis by McComas et al. on the effects of this pressure change on ENA fluxes observed at 1 au using a three-dimensional, time-dependent simulation of the heliosphere. The pressure front has likely already crossed the termination shock (TS) in all directions, but ENA fluxes observed at 1 au will change over the coming years, as the TS, heliopause, and IHS plasma pressure continue to change in response to the SW pressure increase. Taken in isolation, the pressure front creates a "ring" of increasing ENA fluxes projected in the sky that expands in angular radius over time, as a function of the distances to the heliosphere boundaries and the ENA propagation speed. By tracking the position of this ring over time in our simulation, we demonstrate a method for estimating the distances to the TS, heliopause, and ENA source region that can be applied to *IBEX* data. This will require *IBEX* observations at 4.3 keV up through ∼2020, and longer times at lower ENA energies, in order to observe significant changes from the heliotail.

Key words: ISM: atoms – magnetohydrodynamics (MHD) – solar wind – Sun: activity – Sun: heliosphere

1. Introduction

In-ecliptic observations of the solar wind (SW) by *ACE* and *Wind* revealed a relatively sudden increase in SW dynamic pressure in late 2014 (see, e.g., McComas et al. 2018, Figure 1). The SW dynamic pressure ($m_p n_p u^2$, including protons and alpha particles) before the increase was 1.64 nPa (average from ∼2010 to 2014.5). By 2015, the dynamic pressure increased to 2.41 nPa (average from ∼2015 to 2017). This change in SW dynamic pressure was predicted to have a significant effect on the outer heliosphere (McComas et al. 2017), which was observed later in 2017 by the *Interstellar Boundary Explorer* (*IBEX*; McComas et al. 2009a) via measurements of energetic neutral atoms (ENAs; McComas et al. 2018).

IBEX is an Earth-orbiting spacecraft that detects neutral atoms (mainly hydrogen) coming from the outer heliosphere (McComas et al. 2009b). These neutral atoms originate from the very local interstellar medium (VLISM; e.g., Möbius et al. 2009; Bochsler et al. 2012; Rodríguez Moreno et al. 2013; also see review in McComas et al. 2017) or ENAs produced by charge-exchange between SW ions and interstellar neutral atoms in the inner heliosheath (IHS) or outside the heliopause (e.g., Gruntman et al. 2001; Heerikhuisen et al. 2008; Prested et al. 2008; McComas et al. 2009b; also see review in Zank 2015). The hydrogen ENA fluxes observed by *IBEX* depend on the properties of the plasma and neutral atom populations in different regions of the heliosphere, and how these populations interact (e.g., Zank 1999).

McComas et al. (2018) provided the first analysis of *IBEX* observations of the heliosphere's reaction to a dramatic, and relatively sudden, increase in SW dynamic pressure. ENAs observed at *IBEX*' s highest energy bin (∼4.3 keV) were the first to reflect a change, centered approximately ∼30° southward of the nose. At lower energies (∼1.7 and 2.7 keV), the ENA fluxes increased less, and no visible change was observed at the lowest energies (∼0.7 and 1.1 keV) where the ribbon flux appears to be unchanged. McComas et al. (2018) substantiated the interpretation of the observations using a simulation of the SW-VLISM interaction, modeling the SW dynamic pressure increase, and computing its effect on ENA fluxes at 1 au. The simulation confirmed that an increase in the highest energy ENAs occurs first due to their faster propagation, followed by an increase at lower energies with smaller changes.

In this paper, we expand on the simulation results presented in McComas et al. (2018) to better understand how the heliosphere changes due to the SW dynamic pressure increase, how it affects ENA fluxes at 1 au, and how we can use these observations to better understand the heliosphere.

2. Simulating the Increase in SW Dynamic Pressure in Late 2014

Figure 1 shows the SW pressure increase observed at 1 au (OMNI data taken from ftp://spdf.gsfc.nasa.gov/pub/data/omni). From ∼2010 to early 2014, the SW dynamic pressure was approximately stable at 1.6 nPa. In late 2014, the dynamic pressure increased by ∼50% over a span of 6 months. Using a three-dimensional (3D), time-dependent simulation of the SW-VLISM interaction, McComas et al. (2018) modeled this pressure change by introducing a step function increase in SW dynamic pressure in the simulation, with an increase in speed from 406 to 442 km s^{-1}, and density from 5.94 to 7.37 cm^{-3} (note that this density includes protons and alpha particles). While this implementation is simpler than reality, the model showed qualitatively similar behavior in the returning ENA

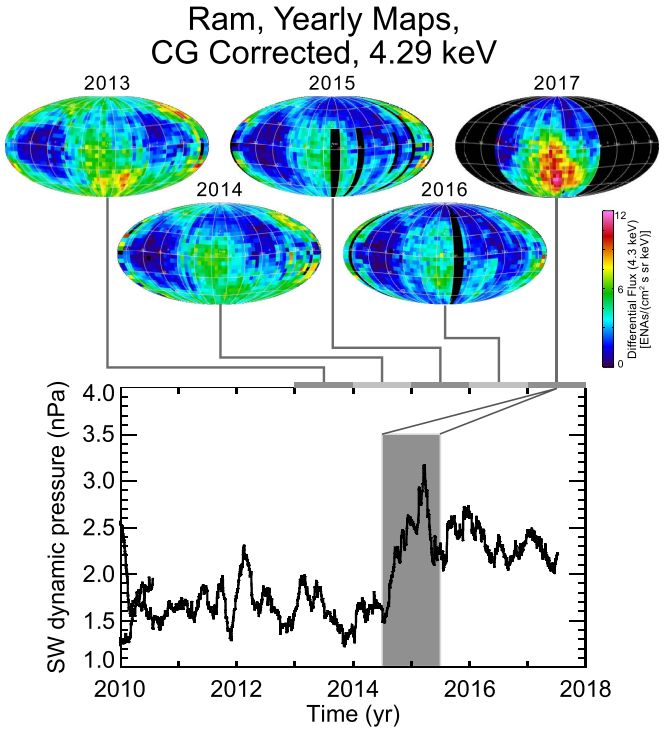

Figure 1. (Top panel) *IBEX* observations of ENAs at 4.3 keV from 2013 to 2017. (Bottom panel) SW dynamic pressure at 1 au. The large increase in SW pressure in late 2014 (dark gray shaded region) is observed in *IBEX* ENA observations ∼2 years later. Adapted from McComas et al. (2018).

fluxes at 1 au, with a sudden change in 4.3 keV ENAs by early 2017 and predicting a delayed and less significant change at lower ENA energies.

We continue the analysis of the simulation from McComas et al. (2018) using the same 3D plasma-neutral code. The code solves MHD equations for the plasma and Boltzmann's equation for neutral hydrogen (Pogorelov et al. 2008). The VLISM boundary conditions use the pristine interstellar magnetic field derived from the analysis of the *IBEX* ribbon by Zirnstein et al. (2016b), with pristine magnitude 2.93 μG and direction (227.°28, 34.°62), which produces a draped magnetic field that agrees well with *Voyager 1* observations outside of the heliopause. The VLISM plasma temperature is 7500 K and flow speed is 25.4 km s^{-1} (McComas et al. 2015), and proton and neutral hydrogen densities are 0.07 and 0.13 cm^{-3}, respectively, which result in a heliopause distance close to that observed by *Voyager 1* before the pressure increase (∼120 au in the *Voyager 1* direction). The SW boundary conditions at 1 au before and after the change in SW dynamic pressure are listed in Table 1, consistent with time-averaged OMNI data. For simplicity, we do not change the SW temperature or magnetic field. Note that the solar magnetic field is unipolar in the simulation, which we choose to implement in order to eliminate an artificially flat heliospheric current sheet and spurious numerical reconnection at the heliopause.

To simulate this SW event, first we iterate the plasma and neutral modules consecutively using the initial SW conditions in order to reach a steady-state solution. Then, we introduce a step function increase in SW density and speed. We continue the simulation for 8 years after the change in SW conditions (∼2023). Finally, we use the time-dependent ENA solver from Zirnstein et al. (2017b) to post-process the heliosphere

Table 1
SW Simulation Parameters at 1 au before and after the SW Pressure Increase in 2014

	Before	After
n_p (cm^{-3})	5.94	7.37
u_p (km s^{-1})	406	442
T_p (K)	51,100	51,100
$\|B\|$ (μG)	37.5 (B_r)	37.5 (B_r)

simulation results in order to compute time-dependent ENA fluxes at 1 au (see Zirnstein et al. 2017b for more details).

We note that the simulation's SW boundary conditions we apply are latitude-independent, which is generally not valid near solar minimum when fast SW propagates outwards from large polar coronal holes (e.g., McComas et al. 2000). Therefore, when performing analyses of our simulation results in Section 4, we limit our calculations to low latitudes. More sophisticated simulations of the latitudinal SW structure in the heliosphere (e.g., Pogorelov et al. 2013; Kim et al. 2016) will be subject of a future study.

2.1. Simulation of the Heliosphere

In Figure 2, we show snapshots in time of the simulation plasma thermal pressure ($n_p k_B T_p$), in steps of 1 year in the solar equatorial plane. Before the SW dynamic pressure changes (0 year), the simulated heliosphere is in a steady-state. One year after the pressure increase, the pressure front has already crossed the TS at the nose-ward side of the heliosphere, propagating approximately halfway through the IHS. Because the distance to the TS is asymmetric, the pressure front has not yet reached the TS near the flanks and tail. After two years have passed, the pressure front has reached the closest point to the heliopause, producing a wave reflected back to the TS, and a pressure wave transmitted across the heliopause and that propagates through the VLISM. Meanwhile, in the direction of the heliotail, the pressure front has already crossed the TS.

Within two years after the SW dynamic pressure increased near the Sun, the plasma pressure in the upwind (with respect to the VLISM flow direction) side of the IHS has increased dramatically (∼40%–50%). The TS and heliopause continue to move outwards from the Sun for at least 7 years after the pressure increase, and the pressure wave transmitted across the heliopause continues to propagate through the VLISM. It takes significantly longer for the pressure to reach a new equilibrium near the flanks and tail of the heliosphere.

3. Simulation of ENA Fluxes at 1 au

3.1. The First Response—4.3 keV ENAs

In this section, we show how the dynamical changes occurring in the IHS affect ENA fluxes at 1 au over time. Figures 3–5 show results for 4.3 keV ENA fluxes from ∼1 to 4 years after the SW dynamic pressure increase. Instead of showing sky maps of the absolute ENA flux, we show the percent change in ENA flux in steps of 3 months. This allows us to better visualize the changes in ENA fluxes over time due to the asymmetry of the distances to the TS and heliopause as the pressure front propagates through the heliosphere.

For example, in Figure 3, we show what the initial effects on ENA fluxes look like. The first panel (0.75–1 years after the SW pressure change) shows no significant change since ENAs

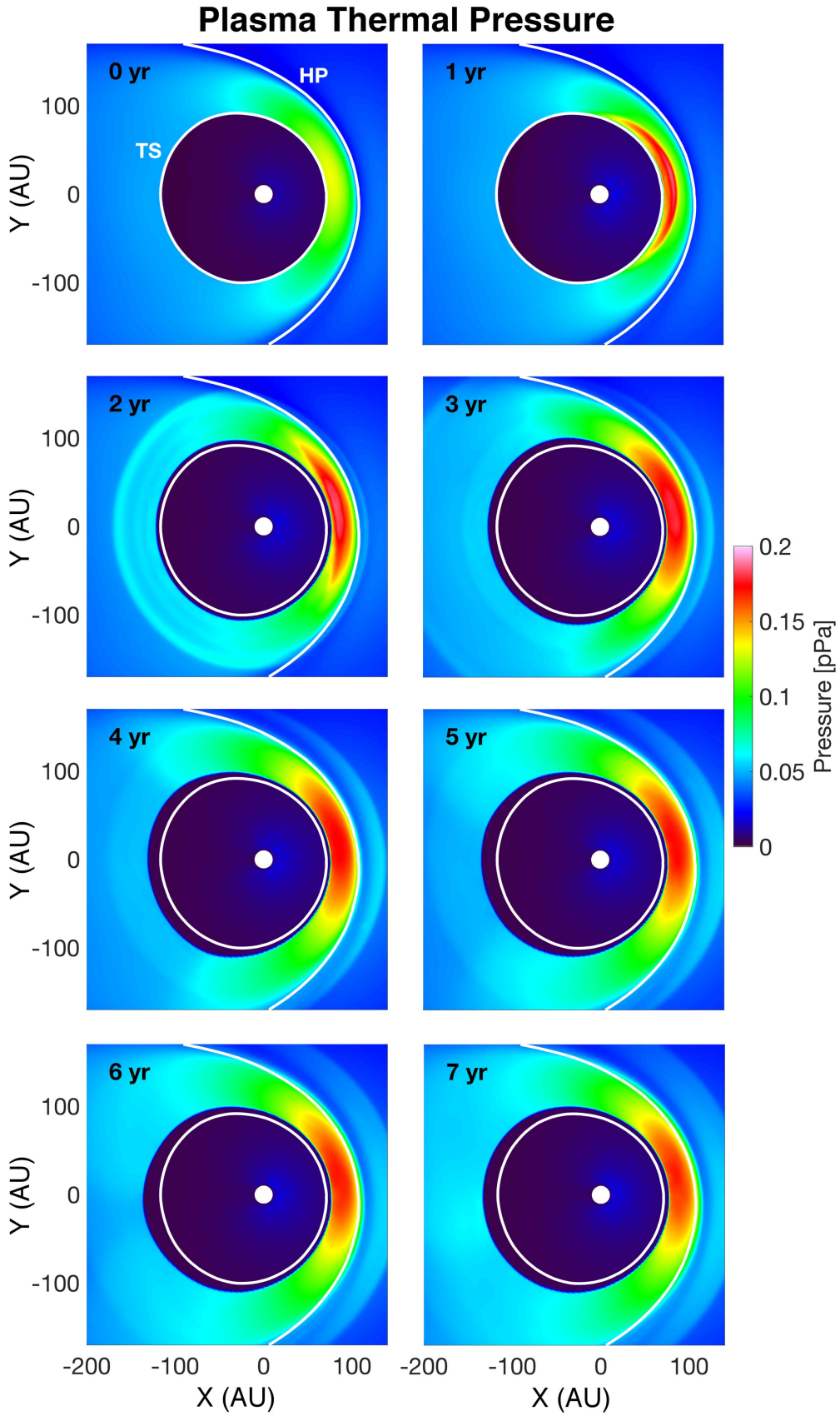

Figure 2. Snapshots of the simulation plasma thermal pressure in the IHS ($n_p k_B T_p$) in steps of 1 year. The snapshots are taken in the solar equatorial plane. The TS and heliopause (HP) surfaces are shown in white for year 0 in every panel, to show the change in their position with time.

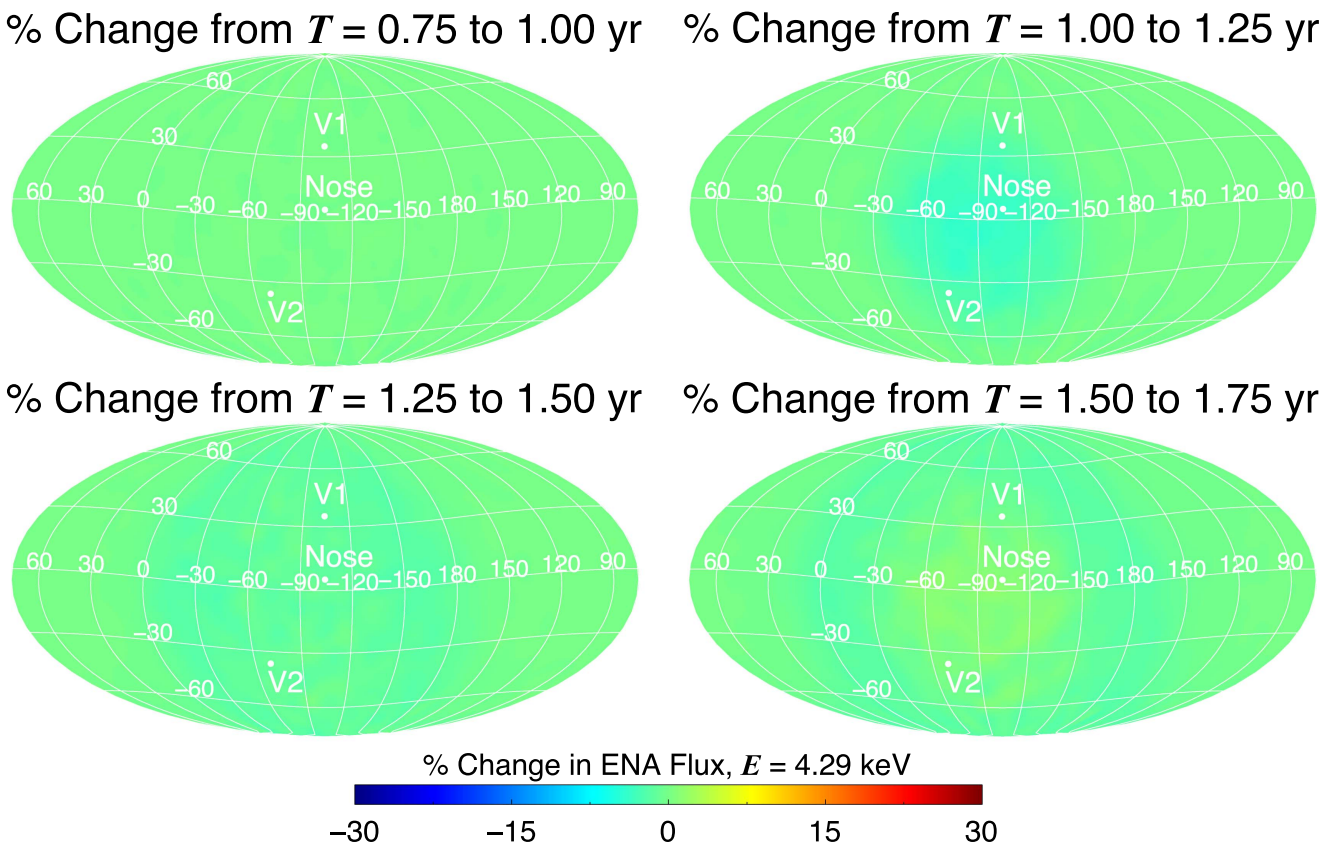

Figure 3. Percent change in ENA flux at 4.3 keV from 1 to 2 years after the SW pressure increase at 1 au. Changes are calculated in steps of 0.25 years.

have not yet returned to 1 au, even though the pressure front has already propagated past the TS at the closest point (see Figure 2). In the next panel (1–1.25 years after), there is a slight reduction in ENA fluxes just below the nose of the heliosphere. This is an interesting, and somewhat unexpected, result that is caused by the outward motion of the TS in response to an increase in SW dynamic pressure. As the pressure front reaches the TS, the TS moves away from the Sun by a few au within the first year. The majority of ENAs have not yet been affected by the pressure change, but the line-of-sight thickness of the ENA source region (i.e., the IHS) has reduced by a few percent, thus resulting in a reduction of the line-of-sight integrated ENA flux at 1 au. This reduction then occurs at larger angles away from the closest point, as the pressure front travels to the farther-distanced TS. Only by ∼1.75 years after the start of the pressure increase do we begin to see an increase in 4.3 keV ENA fluxes once the IHS plasma pressure has reacted (see Figure 2), which corresponds to a measurement time of ∼2016.5.

Figure 4 shows the initial, significant increase in 4.3 keV ENA fluxes from directions centered approximately ∼10° southward and ∼10° port-ward of the nose (leftward in these plots). Over the next 6 months (2–2.5 years after the pressure increase), the 4.3 keV ENA fluxes increase by >20% near the closest point to the TS, and fluxes at slightly larger angles begin to increase later in time. Finally, ∼2.5 years after the pressure increase at 1 au, the ENA fluxes begin to increase at angles >60°, producing a "ring" centered around the apex of the simulation heliosphere ∼(270°, −6°).

Corroborating the prediction from McComas et al. (2017), over time this ring expands in angular radius as the pressure front reaches the TS and propagates through the IHS at directions near the flanks and tail of the heliosphere. As the pressure wave propagates down the flanks of the heliosphere, it must fill a larger volume in the IHS over an extended period of time, resulting in ENA fluxes that do not change as significantly in directions near the flanks and tail as they do near the nose.

This can be seen in Figure 5, which shows the percent change in 4.3 keV ENA fluxes from ∼3 to 4 years after the initial SW pressure increase at 1 au. The pressure front has already crossed the TS in every direction, and the pressure front has begun to reflect from the heliopause and move toward a new equilibrium. It is interesting to note at this point that the rate at which this ENA ring moves across the sky is directly related to the asymmetry of the heliospheric structure. This correlation will be demonstrated in Section 3.3.

3.2. Energy-dependent Response of ENAs

Changes in the IHS plasma are also reflected at lower ENA energies, although later in time due to their slower propagation back toward 1 au. In Figure 6, we compare sky maps of the percent change in ENA flux over several 3-month periods (2–2.25 years, 3–3.25 years, and 4–4.25 years after the SW pressure increase began), for ENA energies 0.7, 1.7, and 4.3 keV. After two years, 4.3 keV ENA fluxes increased significantly near the nose of the heliosphere, whereas a smaller increase occurs at 1.7 keV. At 0.7 keV, no increase is yet observed in ENA fluxes, and a decrease (∼7%) due to the outward motion of the TS is visible. This behavior was identified in simulations by McComas et al. (2018), and should be visible at all ENA energies.

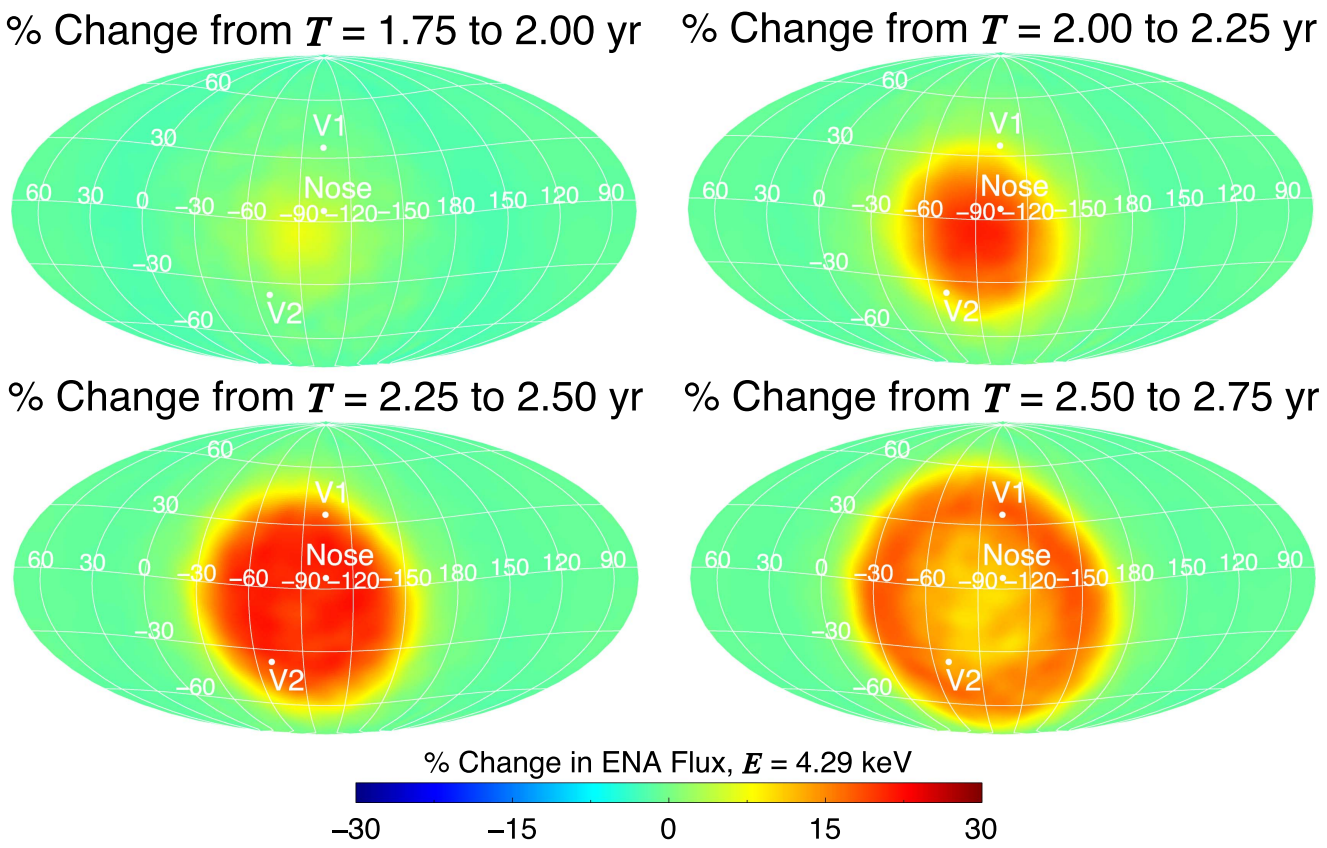

Figure 4. Similar to Figure 3, except changes are from ∼2 to 3 years after the SW pressure increase.

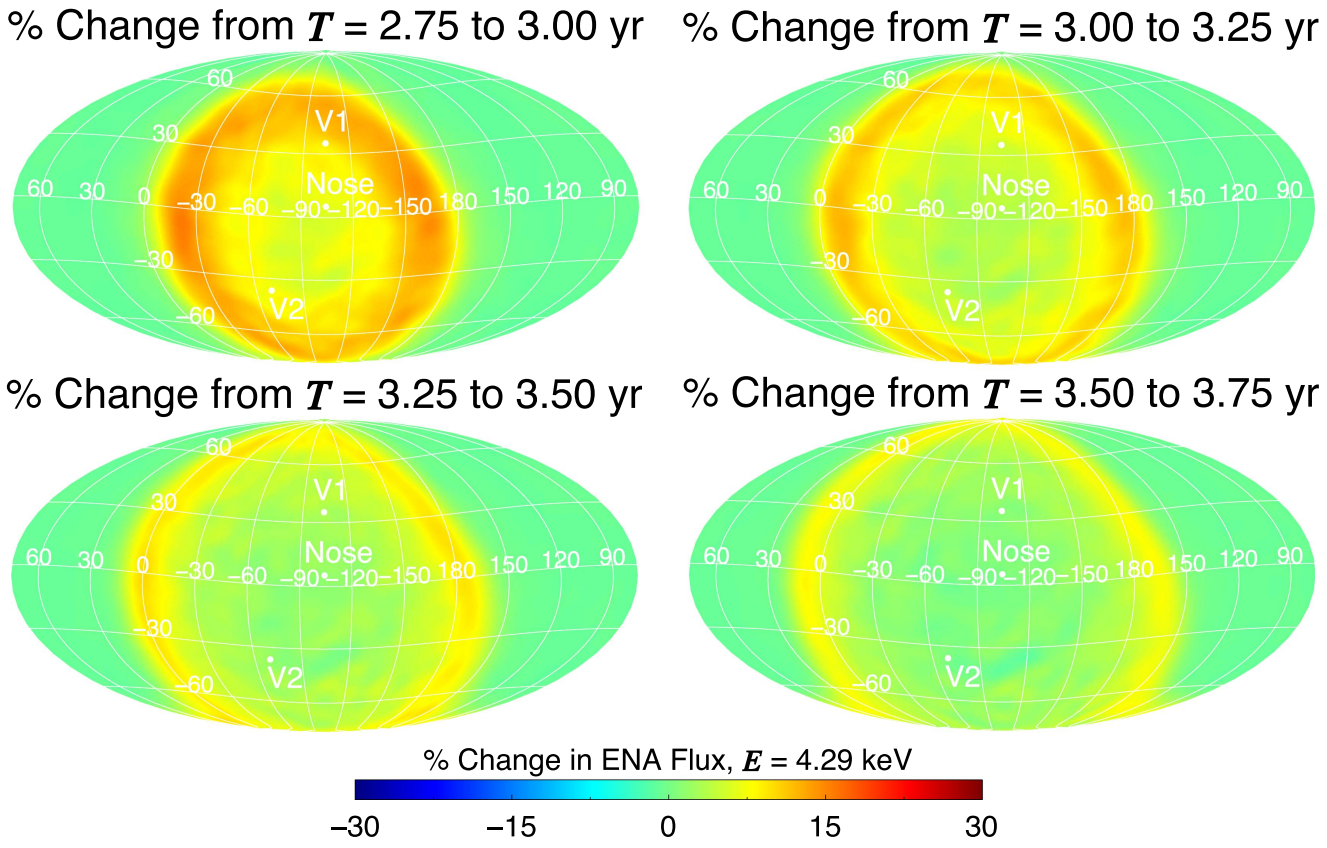

Figure 5. Similar to Figure 3, except changes are from ∼3 to 4 years after the SW pressure increase.

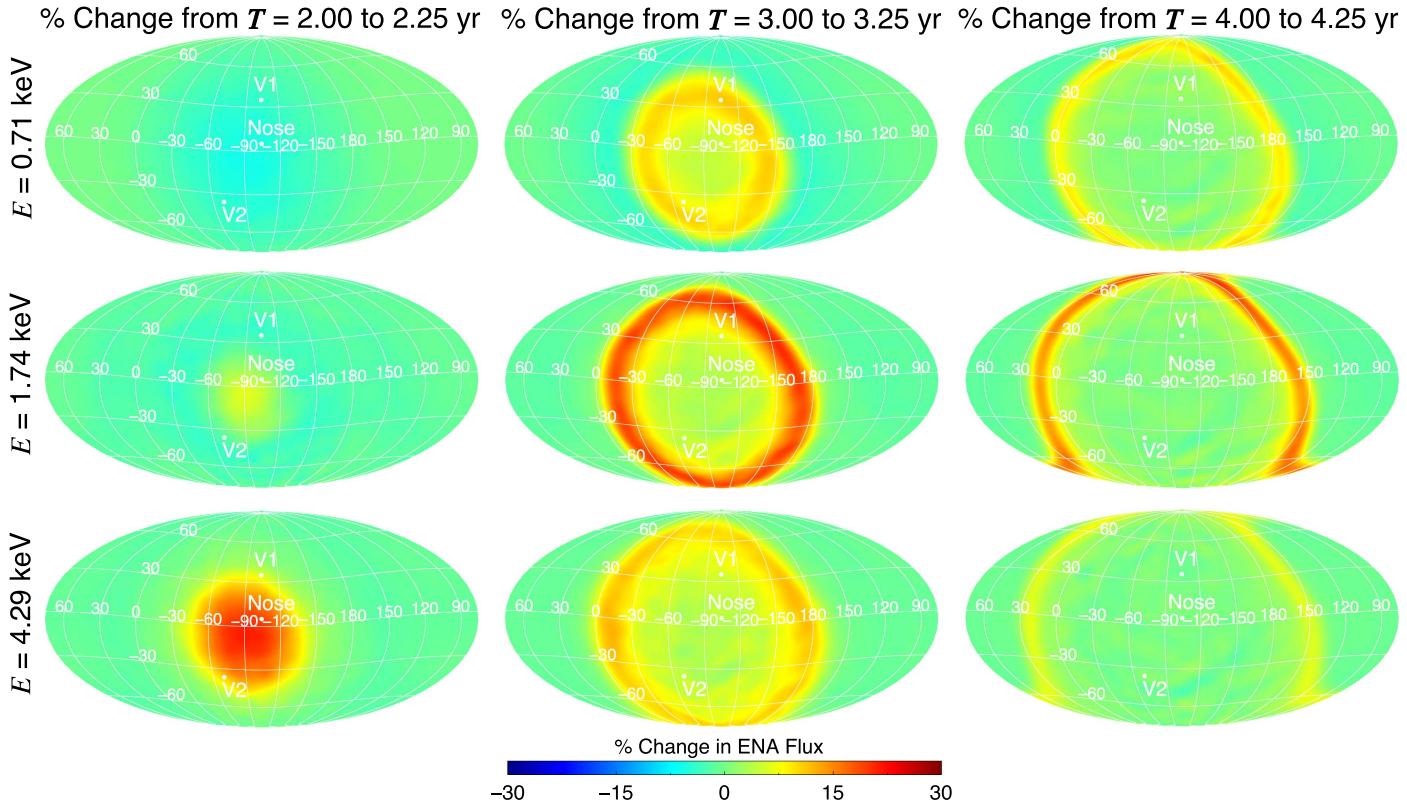

Figure 6. Percent change in ENA flux at 0.7 (top row), 1.7 (middle row), and 4.3 keV (bottom row) from 2 to 2.25 years (left column), 3 to 3.25 years (middle column), and 4 to 4.25 years (right column) after the SW pressure increase.

In the middle column of Figure 6, we show changes in ENA fluxes that occur over a 3-month span from 3 to 3.25 years after the SW pressure increase. At the highest ENA energy, we see the ring of increasing ENA flux propagating away at large angles from the initial point. The change in 1.7 keV ENAs is delayed in time, resulting in a smaller ring at this time, and the 0.7 keV ENAs are delayed even longer. Finally, in the right column of Figure 6 (changes from 4 to 4.25 years after the pressure increase), the change in ENA fluxes have propagated toward the flanks, as a function of ENA energy. Although it is not shown here, the ring of increasing ENA flux propagates all the way to the tail within ∼6 years after the SW pressure increase for 4.3 keV ENAs, and considerably longer for lower energies.

3.3. Determining the Distances to the Heliospheric Boundaries

In the previous section, we showed how an abrupt increase in SW dynamic pressure propagates to the outer heliosphere and affects ENA fluxes at 1 au as a function of energy and time. The response of these ENAs not only depends on their energy, but also on the asymmetric distances to the TS, heliopause, and ENA source region (e.g., Zirnstein et al. 2016a, 2017b). In this section, using our simulation, we demonstrate how one can estimate the distances to these heliosphere boundaries using ENA observations at 1 au and illustrate the range of assumptions one may use to calculate the distances to the heliospheric boundaries, which may or may not result in accurate results.

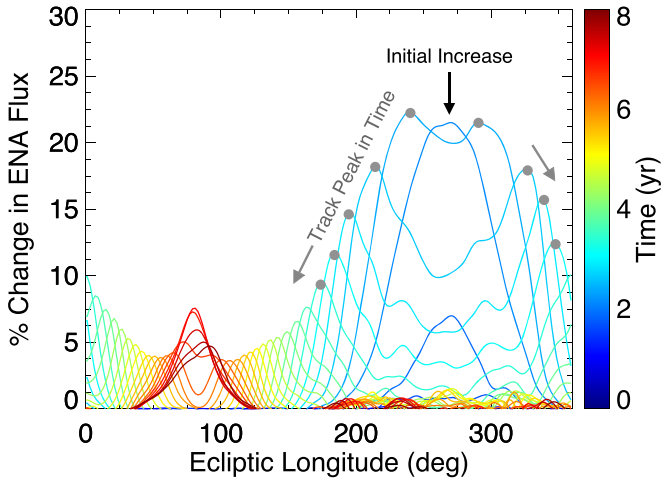

Figure 7. Percent change in simulated 4.3 keV ENA flux at ecliptic latitude −6°, as a function of ecliptic longitude and time. We track the peak change in ENA flux (gray dots) in time as a function of angle from the initial increase position in order to determine the distances to the heliospheric boundaries.

3.3.1. Deriving the Distance to the TS

We can estimate the distance to the TS by tracking the ring of increasing ENA flux as a function of angle from the direction where the fluxes initially increased. Figure 7 shows the simulated 4.3 keV ENA flux at 1 au as a function of ecliptic longitude at ecliptic latitude −6°. The initial increase occurred from direction ∼(270°, −6°), approximately 2 years after the SW pressure increased at the Sun. As time progresses, the peak change in simulated ENA flux observed from longitude 270° at

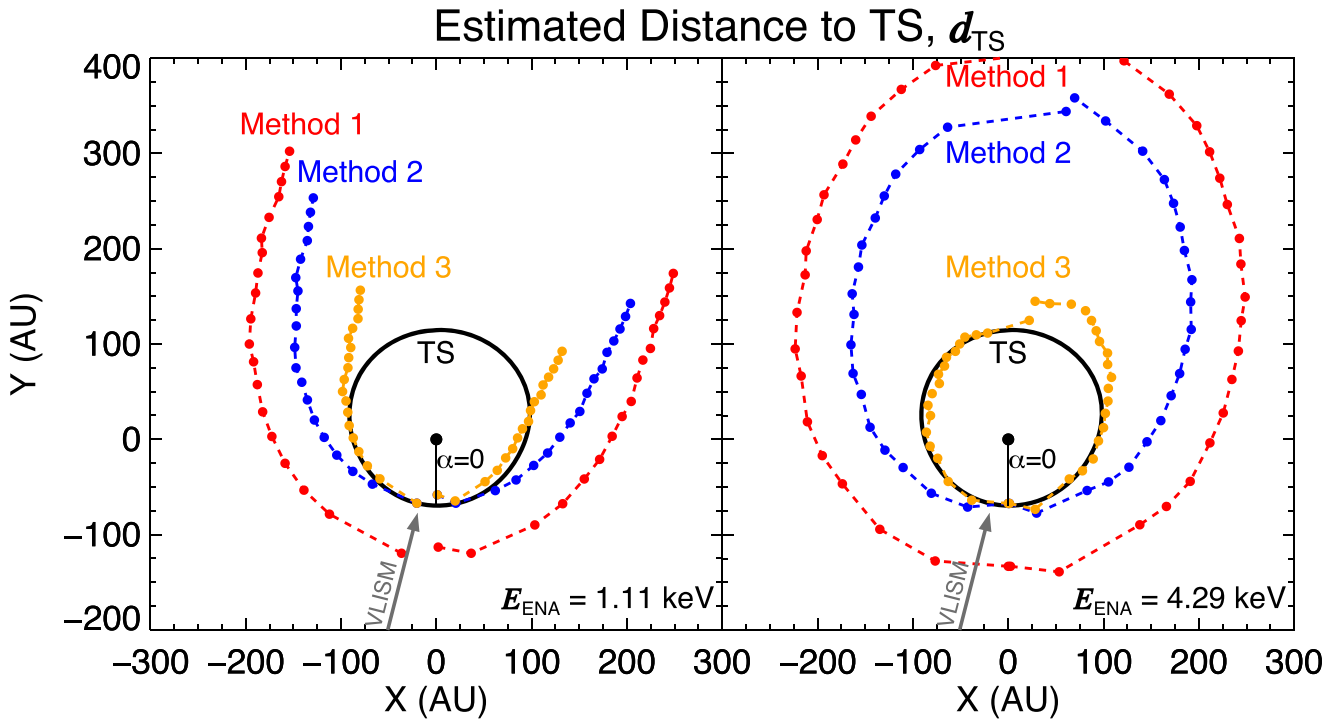

Figure 8. Estimations of the distance to the TS in our simulation at ecliptic latitude −6° based on directions of the peak change in ENA flux over time for 1.1 keV (left) and 4.3 keV (right) ENAs. The actual distance to the TS from the simulation before the pressure pulse occurred is shown in black, whereas three different methods for calculating the distance are shown as colored dashed lines (Method 1—red, Method 2—blue, Method 3—orange).

1 au expands to either side as the pressure front propagates across the TS at larger angles from the point of initial contact. We track the movement of this peak over time as a function of ecliptic longitude (at the same latitude of −6°).

We investigate multiple techniques of varying complexity to demonstrate how one can derive the distances to the heliospheric boundaries. While we already know the distances to the heliosphere boundaries in our simulation, we will use our simulation results as a test-bed for this demonstration. The first simple assumption we can make is that when the pressure front reaches the TS, the majority of ENA fluxes at this energy are created instantly and begin to propagate back toward 1 au. Thus, we can relate the time for observing the initial increase in ENA fluxes t_{ENA} ($T = 2.125$ in Figure 7) to the distance to the TS d_{TS} (which, again, we assume we do not know from our simulation), as a function of angle α from the initial point of contact of the pressure front with the IHS ($\alpha = 0$), by

$$t_{ENA}(\alpha) = \frac{d_{TS}}{v_{SW}} + \frac{d_{TS}}{v_{ENA}} = d_{TS}(\alpha)\left(\frac{1}{v_{SW}} + \frac{1}{v_{ENA}}\right), \quad (1)$$

where v_{SW} is the supersonic SW speed and v_{ENA} is the ENA speed (assumed to be the nominal speed of ENAs in the center of each *IBEX* energy bin). The first term on the right-hand side of Equation (1) is the time it takes for the supersonic SW to travel from the Sun to the TS. Note that the SW speed decreases with distance from the Sun due to PUI mass loading; however, for the illustrative purposes of this study we assume v_{SW} is constant. The second term is the time it takes for ENAs to travel back to 1 au (which is over distance d_{TS}, which changes with angle α). By relating the time at which we simulate the peak increase in ENA flux at 1 au (see Figure 7) with known supersonic SW speed after the pressure increase (442 km s^{-1}) and ENA speed ($v_{1.1\ keV} = 461$ km s^{-1}, $v_{4.3\ keV} = 907$ km s^{-1}), we can estimate the distance to the TS in our simulation as a function of angle α from the point of closest contact using Equation (1). This is shown as the red curves in Figure 8 ("Method 1").

We can determine how accurate this method is by extracting the actual distance to the TS in these directions from our MHD simulation before the pressure increase reached the TS. The actual distances are shown alongside the results in Figure 8 (black curves). As expected, this method is not accurate in reproducing the distance to the TS. The distances are overestimated because, in reality, more time is taken for the SW pressure front to propagate through the IHS and for ENAs to propagate back from the IHS to Earth.

Next, we can improve this method by including additional terms in Equation (1) that account for the flow speed of a pressure wave traveling through the IHS, as well as for the extra time it takes ENAs to propagate through the IHS back toward 1 au, similar to that done by Reisenfeld et al. (2016). Equation (1) now becomes

$$\begin{aligned} t_{ENA}(\alpha) &= \frac{d_{TS}}{v_{SW}} + \frac{3}{2}\frac{l_{IHS}}{v_{ms}} + \frac{d_{TS}}{v_{ENA}} + \frac{1}{2}\frac{l_{IHS}}{v_{ENA}} \\ &= d_{TS}(\alpha)\left(\frac{1}{v_{SW}} + \frac{1}{v_{ENA}}\right) + l_{IHS}\left(\frac{3}{2v_{ms}} + \frac{1}{2v_{ENA}}\right), \end{aligned} \quad (2)$$

where l_{IHS} is an unknown distance through the IHS, and v_{ms} is the magnetosonic wave speed in the IHS. McComas et al. (2018) found that the majority of ENAs increase in intensity after the pressure wave traveled to the heliopause and partially reflected back toward the TS. Only after the pressure wave propagates to the heliopause and "pushes back" can the plasma

pressure in the IHS readjust to its new, higher, level. Thus, the second term on the right-hand side of Equation (2) approximately accounts for the time it takes the pressure wave to travel to the heliopause and reflect back toward the TS to a distance where the majority of ENAs are created, which we assume to be halfway through the IHS. Thus, this yields a total distance to travel of $3/2\ l_{\rm IHS}$. The fourth term accounts for the time it takes ENAs to travel from halfway through the IHS to the TS, which we estimate as the average distance through the ENA source region (see, e.g., Zirnstein et al. 2016a). In this demonstration, we assume that the wave speed in the IHS ($v_{\rm ms} = 300$ km s^{-1}) and the distance from the TS to the heliopause ($l_{\rm IHS} = 40$ au) are constant and independent of angle α. Both are derived from our MHD simulation for the speed of the wave and the initial thickness of the IHS in the front of the heliosphere. After solving Equation (2) with these assumptions, we compare to the actual distance to the TS from the simulation in Figure 8 ("Method 2"). As shown, this compares significantly better than Method 1 to the actual distances near ecliptic longitude 270° where the initial increase occurred ($\alpha \sim 0$), as at this location, the thickness of the IHS is approximately 40 au. Thus, this shows that at least near the front of the heliosphere, the majority of ~4.3 keV ENA fluxes react after the pressure front has propagated through the entire IHS and reflected part-way back toward the TS, and $l_{\rm IHS}$ represents the thickness of the IHS. However, this method performs poorly near the flanks and tail of the heliosphere, likely as $l_{\rm IHS}$ is not really the same in every direction.

To improve this, we remove the assumption that the pressure wave must only travel a fixed distance through the IHS (i.e., $l_{\rm IHS}$—is no longer constant) and allow $l_{\rm IHS}$ to increase as a function of angle from the closest point of contact of the pressure front. This is a more realistic assumption as (1) the distance to the heliopause increases as a function of angle from the closest point, and (2) it has been shown in prior simulations that the ENA source region increases in thickness at larger angles from the nose (see, e.g., Figure 8 from Zirnstein et al. 2016a). We modify Equation (2) by defining the term $l_{\rm IHS}$ to increase with angle α, as the effective depth at which ENAs are created as a function of angle from the initial direction,

$$l_{\rm IHS}(\alpha) = l_{\rm IHS,0} \exp\left(A[\Delta\alpha]^{\gamma}\right), \quad (3)$$

where $l_{\rm IHS,0} = 40$ au, A and γ are constant free parameters, and $\Delta\alpha$ is the angular distance from the initial point. We choose the particular functional form in Equation (3) merely such that $l_{\rm IHS}$ increases nonlinearly with angle (other functions could be used, e.g., Zirnstein et al. 2016a, but Equation (3) yields reasonable results at 4.3 keV in Figure 8). By comparing to the actual distances from the simulation, we find a good comparison when $A = 7 \times 10^{-4}$ and $\gamma = 1.5$ ("Method 3"). We perform the same analysis for 1.1 and 4.3 keV ENAs in Figure 8. Note that all parameters for each method are listed in Table 2.

Figure 8 shows that, of the three cases we demonstrated, Method 3 produces the best estimation of the distance to the TS. The results for both 1.1 and 4.3 keV are fairly accurate in the upwind hemisphere of the heliosphere (within ~100°). However, in the downwind hemisphere, the estimated distance to the TS using 1.1 keV ENAs overestimates the actual distance, while the results for 4.3 keV match well only on the starboard side of the TS ($-x$ axis).

Table 2
Parameters for Determining the Distance to the TS

	Method 1	Method 2	Method 3
$v_{\rm ENA}$ (km s^{-1})[a]	907	907	907
$v_{\rm SW}$ (km s^{-1})[b]	442	442	442
$v_{\rm ms}$ (km s^{-1})[c]	⋯	300	300
l_0 (au)[d]	⋯	40	40
A (deg$^{-\gamma}$)[e]	⋯	0	7×10^{-4}
γ[f]	⋯	⋯	1.5

Notes.
[a] Speed of 4.3 keV ENA.
[b] Magnetosonic wave speed in the IHS.
[c] SW speed ahead of the TS after the pressure increase.
[d] Minimum thickness of the IHS.
[e] Extra distance in the IHS.
[f] Constants used in Equation (4).

The differences between the results for 1.1 and 4.3 keV for Method 3 highlight one of the main reasons for demonstrating these calculations. This discrepancy is due to our choice of the parameters for $l_{\rm IHS}(\alpha)$ to best match the 4.3 keV ENA results. It implies that the distances we assumed for $l_{\rm IHS}$ (Equation (3), Table 2) near the heliotail for 1.1 keV ENAs were too small, underestimating the amount of time it takes for the majority of 1.1 keV ENAs affected by the pressure change to be observed at 1 au. This is understandable because lower energy ENAs can be produced at farther distances from the TS, due to the energy-dependent charge-exchange process (see, e.g., Zirnstein et al. 2016a, 2017b). Interestingly, the results for 4.3 keV on the port side of the TS ($+x$ axis) overestimate the distance to the TS near the heliotail, a consequence of asymmetric plasma properties in the IHS, likely related to the asymmetric interstellar magnetic field pressure on the heliopause.

3.3.2. Deriving the Distance to the Heliopause and ENA Source

In this section, we demonstrate how one can derive the distance to the heliopause and ENA source in the IHS using our simulated observations of the change in ENA fluxes at 1 au. Deriving the IHS thickness is a more valuable calculation, as various heliospheric models compute more consistent distances to the TS, but not consistent distances to the heliopause (e.g., Izmodenov & Alexashov 2015; Opher et al. 2015, 2016; Pogorelov et al. 2015; Pogorelov 2016). In order to solve Equation (2) directly for $l_{\rm IHS}$, we need to know (1) the distance to the TS, and (2) the time it takes for the ENAs to respond to the pressure increase as a function of angle from the initial point. The latter can be achieved by utilizing *IBEX* observations over the coming years to track the peak change in ENA flux due to the pressure increase (note that in this study, we use our simulation results). The former is more complex, but global simulations of the heliosphere can be used to estimate the TS distances. For this demonstration, we use the actual distance to the TS from our simulation, for simplicity. As $d_{\rm TS}$ is calculated directly from our simulation, and the timing of the change in the peak ENA flux, i.e., ring, observed at 1 au is used for $t_{\rm ENA}$, we can solve Equation (2) for $l_{\rm IHS}$. The results are shown in

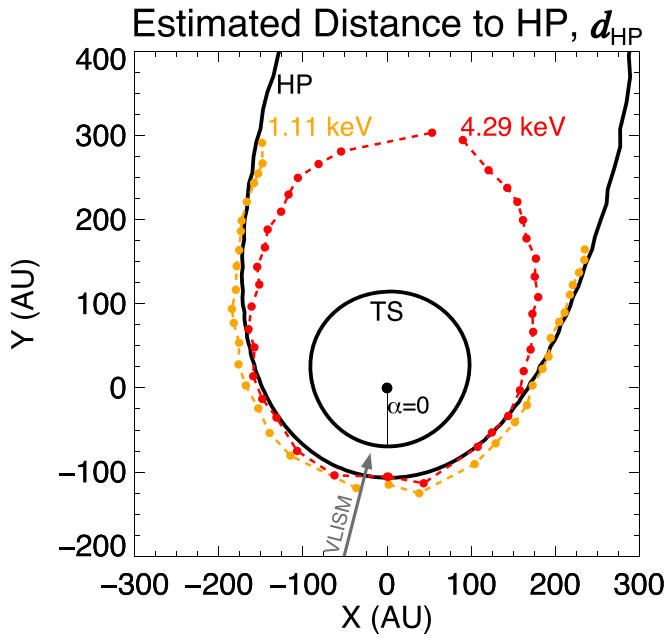

Figure 9. Estimation of the distance to the heliopause in our simulation ($d_{HP} = d_{TS} + l_{IHS}$) using Method 3, derived from solving Equations (2) and (3). Note that this is not the same as the ENA cooling length, which is smaller in scale.

Figure 9, for 1.1 and 4.3 keV ENAs. We plot the actual distance to the TS from our simulation and heliopause (black curves), and the results from calculating l_{IHS}. Note that we add $d_{TS} + l_{IHS} = d_{HP}$ in Figure 9 to show the estimated distance to the heliopause, d_{HP}.

As can be seen in Figure 9, the distance d_{HP} is close to the actual simulated heliopause at the front side of the heliosphere (note that the black curves represent the distances to the TS and heliopause before the pressure pulse reached the TS in the simulation). This is because there are a significant number of sunward-directed ENAs produced everywhere in the IHS, even though there is an extinction of ∼keV PUIs by charge-exchange as the plasma flows through the heliosheath (Lindsay & Stebbings 2005). At larger angles from the nose, the distance to the heliopause increases, and d_{HP} increases similarly. While d_{HP} for 1.1 keV is approximately consistent with the distance to the heliopause for most of the data set, d_{HP} for 4.3 keV is shorter toward the heliotail. This is partly due to the limited ENA source depth caused by the extinction of ∼4 keV PUIs (e.g., Schwadron et al. 2014; Zirnstein et al. 2016a) due to the energy-dependent, charge-exchange cross section (Lindsay & Stebbings 2005). However, d_{HP} presented in Figure 9 is somewhat larger than the ENA "cooling length" distance past the TS derived in previous studies (see, e.g., Zirnstein et al. 2016a, Figure 8). This is likely related to the constraints we impose in Equation (2). The time it takes for the pressure front to make significant changes to the ENA source populations is likely not as simple as Equation (2) assumes. However, the results presented in Figure 9 strongly suggest that this equation is quite robust in informing us of the approximate distance to the heliopause when using the lower ENA energy observations, and a minimum distance for higher ENA energies near the heliotail.

Thus, by using our simulation of the increase in SW dynamic pressure in late 2014 and the delayed changes in ENA fluxes at 1 au, we show that future *IBEX* observations of the change in ENA fluxes from the heliosphere will provide an independent means for estimating the thickness of the IHS both near the front, flanks, and at least a minimum distance to the heliopause in the heliotail.

4. Discussion and Conclusion

An abrupt and significant increase in SW dynamic pressure by ∼50% was observed at 1 au in late 2014 (Figure 1). This pressure front propagated to the outer heliosphere, crossed the TS in 2015, and created an increased plasma pressure in the IHS (Figure 2). This increase in plasma pressure generated a time-dependent increase in ENAs observed at 1 au by *IBEX* (McComas et al. 2018). We expand on the work of McComas et al. (2018) by analyzing the effects of the pressure change in the heliosphere, and the resulting change in ENA fluxes at 1 au. We utilize a 3D, time-dependent simulation of the heliosphere to model the SW conditions and a time-dependent ENA solver to compute ENA fluxes at 1 au.

As was described by McComas et al. (2018), the direction in the sky where the pressure front reaches the TS first is its closest position to the Sun. This is approximately toward ecliptic (270°, −6°) in our simulation. After the pressure front reaches the TS, the TS begins to move away from the Sun due to the increase in upstream dynamic pressure, resulting initially in a small decrease of ENAs observed at 1 au due to the decrease in the thickness of the IHS (i.e., the line-of-sight integrated source of ENAs is decreased). Then, after the pressure wave propagates to the heliopause, part of the wave is reflected and travels back toward the TS, while the remainder is transmitted past the heliopause into the VLISM (see also, e.g., Pogorelov et al. 2009, 2013; Kim et al. 2017; Washimi et al. 2017, and references therein). The partial reflection of the wave and the flow of plasma with higher pressure across the TS and through the IHS results in an average increase in the plasma pressure.

Our simulation predicts that within two years of the observed pressure increase at 1 au (late 2016), the pressure front will have crossed the TS in all directions of the sky as it takes less than two years for the supersonic SW to travel ∼150 au. However, while *IBEX* observed an increase in ∼4.3 keV ENAs from near the closest point of the TS in late 2016 (McComas et al. 2018), no significant change has been observed at lower energies (<2 keV), nor any changes at large angles (>60°) away from the nose direction. This suggests that the plasma pressure in the flanks and tail of the IHS has not yet adjusted to the change in SW dynamic pressure.

Our simulation corroborates the prediction from McComas et al. (2017) that from late 2017 to early 2018, a "ring" of increasing ENA fluxes (note that this ring is visualized best by creating sky maps of the change in ENA flux over time) at ∼4.3 keV may be observed in the sky, centered on the direction where the TS and heliopause are closest to the Sun, and will expand in angular radius over time as the pressure front travels through the flanks and tail of the IHS. The rate at which it expands in angle across the sky as a function of time depends on the magnetosonic wave speed and the distances to the TS, heliopause, and the regions in the IHS where the majority of ENAs are generated, which are not spatially uniform. Our simulation predicts that *IBEX* will observe the expanding ring from directions near the tail of the heliosphere within ∼6 years of the initial increase in SW pressure observed at 1 au, or in late ∼2020, in the 4.3 keV ENA sky maps. It will take longer for

IBEX to observe a change at lower ENA energies from the heliotail.

We can utilize future *IBEX* observations of this expanding ring of increasing ENA intensity to determine the distances to the heliospheric boundaries. We demonstrated this using our 3D simulation of the heliosphere. By defining a simple, yet realistic, parametric equation that relates the observation time at 1 au of the change in ENA fluxes to the speeds and distances over which the pressure front and ENAs travel, we have shown that it is important to account for (1) the propagation of the pressure wave to the TS, to the heliopause, and its reflection back into the IHS, and (2) the propagation of ENAs approximately halfway within the IHS back to 1 au. We have derived a parametric equation that could be used to estimate the distance to the TS from *IBEX* observations, similar to that used by Reisenfeld et al. (2016) to track changes in ENA fluxes from the ecliptic pole directions. However, we modify the equation to account for the time it takes the IHS to fully respond to a change in the SW dynamic pressure by properly including the IHS pressure wave propagation time.

We have also shown that if one can use other methods to derive the distance to the TS, either using *IBEX* data or by making a reasonable assumption for the TS distance with assistance from a sophisticated 3D simulation of the heliosphere, then *IBEX* observations of the change in ENA fluxes as a function of time due to the SW pressure increase in 2014 can provide a means to determine the distances to the heliopause and ENA source region in many look directions (Figure 9). As the source of ENAs from the IHS is affected by the extinction of energetic protons by charge-exchange (e.g., Zirnstein et al. 2017b), the methods described in this study can give a lower limit to the distance to the heliopause in the direction of the heliotail at the highest ENA energies.

The results presented in this paper assumed that the SW boundary conditions in our simulation were uniform and latitude-independent. However, this is not usually the case. In late 2013, the southern polar coronal hole was starting to open (Karna et al. 2014). This means that faster SW streams will propagate to the outer heliosphere and significantly affect high-energy ENAs at higher latitudes (Reisenfeld et al. 2016; Zirnstein et al. 2017a). Thus, our results are not necessarily valid at higher latitudes, which is the primary reason why we only analyzed the results in Section 3 at low latitudes (note that the analysis will also be complicated by the ribbon flux, which is believed to originate from outside the heliopause; see McComas et al. 2009b, 2017 and references therein). We expect that the latitude and time-dependent SW structure will complicate analyses of *IBEX* data at high latitudes using the methods described here. A more sophisticated simulation of SW conditions would be needed to better understand the effects on ENA fluxes and their relationship with *IBEX* observations at higher latitudes.

E.Z., J.H., and N.P. acknowledge support from NASA grant NNX16AG83G. J.H. and N.P. also acknowledge support from NASA grants NNX14AJ53G, NNX14AF43G, and NNX15AN72G, as well as NSF PRAC award ACI-1144120 and related computer resources from the Blue Waters sustained-petascale computing project. This work was also carried out as part of the *IBEX* mission, which is part of NASA's Explorer program. The work reported in this paper was partially performed at the TIGRESS high performance computer center at Princeton University, which is jointly supported by the Princeton Institute for Computational Science and Engineering and the Princeton University Office of Information Technology's Research Computing department. Supercomputer time allocations were also provided on SGI Pleiades by NASA High-End Computing Program award SMD-16-7570 and Stampede by NSF XSEDE project MCA07S033.

ORCID iDs

E. J. Zirnstein https://orcid.org/0000-0001-7240-0618
D. J. McComas https://orcid.org/0000-0001-6160-1158
N. V. Pogorelov https://orcid.org/0000-0002-6409-2392
D. B. Reisenfeld https://orcid.org/0000-0003-1874-9450
J. R. Szalay https://orcid.org/0000-0003-2685-9801

References

Bochsler, P., Petersen, L., Möbius, E., et al. 2012, ApJS, 198, 13
Gruntman, M., Roelof, E. C., Mitchell, D. G., et al. 2001, JGR, 106, 15767
Heerikhuisen, J., Pogorelov, N. V., Florinski, V., Zank, G. P., & le Roux, J. A. 2008, ApJ, 682, 679
Izmodenov, V. V., & Alexashov, D. B. 2015, ApJS, 220, 32
Karna, N., Hess Webber, S. A., & Pesnell, W. D. 2014, SoPh, 289, 3381
Kim, T. K., Pogorelov, N. V., & Burlaga, L. F. 2017, ApJL, 843, L32
Kim, T. K., Pogorelov, N. V., Zank, G. P., Elliott, H. A., & McComas, D. J. 2016, ApJ, 832, 72
Lindsay, B. G., & Stebbings, R. F. 2005, JGR, 110, A12213
McComas, D. J., Allegrini, F., Bochsler, P., et al. 2009a, SSRv, 146, 11
McComas, D. J., Allegrini, F., Bochsler, P., et al. 2009b, Sci., 326, 959
McComas, D. J., Barraclough, B. L., Funsten, H. O., et al. 2000, JGR, 105, 10419
McComas, D. J., Bzowski, M., Fuselier, S. A., et al. 2015, ApJS, 220, 22
McComas, D. J., Dayeh, M. A., Funsten, H. O., et al. 2018, ApJL, 856, L10
McComas, D. J., Zirnstein, E. J., Bzowski, M., et al. 2017, ApJS, 229, 41
Möbius, E., Bochsler, P., Bzowski, M., et al. 2009, Sci., 326, 969
Opher, M., Drake, J. F., Zieger, B., & Gombosi, T. I. 2015, ApJL, 800, L28
Opher, M., Drake, J. F., Zieger, B., Swisdak, M., & Toth, G. 2016, PhPl, 23, 056501
Pogorelov, N. V. 2016, JPhCS, 719, 012013
Pogorelov, N. V., Borovikov, S. N., Heerikhuisen, J., & Zhang, M. 2015, ApJL, 812, L6
Pogorelov, N. V., Borovikov, S. N., Zank, G. P., & Ogino, T. 2009, ApJ, 696, 1478
Pogorelov, N. V., Suess, S. T., Borovikov, S. N., et al. 2013, ApJ, 772, 2
Pogorelov, N. V., Zank, G. P., Borovikov, S. N., et al. 2008, in ASP Conf. Ser. 385, Numerical Modeling of Space Plasma Flows, ed. N. V. Pogorelov, E. Audit, & G. P. Zank (San Francisco, CA: ASP), 180
Prested, C., Schwadron, N. A., Passuite, J., et al. 2008, JGR, 113, A06102
Reisenfeld, D. B., Bzowski, M., Funsten, H. O., et al. 2016, ApJ, 833, 277
Rodríguez Moreno, D. F., Wurz, P., Saul, L., et al. 2013, A&A, 557, A125
Schwadron, N. A., Moebius, E., Fuselier, S. A., et al. 2014, ApJS, 215, 13
Washimi, H., Tanaka, T., & Zank, G. P. 2017, ApJL, 846, L9
Zank, G. P. 1999, SSRv, 89, 413
Zank, G. P. 2015, ARA&A, 53, 449
Zirnstein, E. J., Dayeh, M. A., McComas, D. J., & Sokół, J. M. 2017a, ApJ, 846, 63
Zirnstein, E. J., Funsten, H. O., Heerikhuisen, J., et al. 2016a, ApJ, 826, 58
Zirnstein, E. J., Heerikhuisen, J., Funsten, H. O., et al. 2016b, ApJL, 818, L18
Zirnstein, E. J., Heerikhuisen, J., Zank, G. P., et al. 2017b, ApJ, 836, 238